

# Understanding the performance differences between solution and vacuum deposited OLEDs: A computational approach

Cite as: J. Chem. Phys. 156, 214703 (2022); <https://doi.org/10.1063/5.0091142>

Submitted: 11 March 2022 • Accepted: 13 May 2022 • Published Online: 01 June 2022

 Stephen Sanderson,  George Vamvounis,  Alan E. Mark, et al.



View Online



Export Citation



CrossMark

Lock-in Amplifiers  
up to 600 MHz



Zurich  
Instruments



# Understanding the performance differences between solution and vacuum deposited OLEDs: A computational approach

Cite as: J. Chem. Phys. 156, 214703 (2022); doi: 10.1063/5.0091142

Submitted: 11 March 2022 • Accepted: 13 May 2022 •

Published Online: 1 June 2022



View Online



Export Citation



CrossMark

Stephen Sanderson,<sup>1</sup>  George Vamvounis,<sup>1</sup>  Alan E. Mark,<sup>2</sup>  Paul L. Burn,<sup>2,3</sup>  Ronald D. White,<sup>1</sup>   
and Bronson W. Philippa<sup>4,a)</sup> 

## AFFILIATIONS

<sup>1</sup> College of Science and Engineering, James Cook University, Townsville, QLD 4811, Australia

<sup>2</sup> School of Chemistry and Molecular Biosciences, The University of Queensland, Brisbane, QLD 4072, Australia

<sup>3</sup> Centre for Organic Photonics & Electronics, The University of Queensland, Brisbane, QLD 4072, Australia

<sup>4</sup> College of Science and Engineering, James Cook University, Cairns, QLD 4878, Australia

<sup>a)</sup> Author to whom correspondence should be addressed: [bronson.philippa@jcu.edu.au](mailto:bronson.philippa@jcu.edu.au)

## ABSTRACT

Solution-processing of organic light-emitting diode films has potential advantages in terms of cost and scalability over vacuum-deposition for large area applications. However, solution processed small molecule films can have lower overall device performance. Here, novel molecular dynamics techniques are developed to enable faster simulation of solvent evaporation that occurs during solution processing and give films of thicknesses relevant to real devices. All-atom molecular dynamics simulations are then used in combination with kinetic Monte Carlo transport modeling to examine how differences in morphology stemming from solution or vacuum film deposition affect charge transport and exciton dynamics in films consisting of light-emitting *bis*(2-phenylpyridine)(acetylacetonate)iridium(III) [Ir(ppy)<sub>2</sub>(acac)] guest molecules in a 4,4'-bis(*N*-carbazolyl)biphenyl host. While the structures of the films deposited from vacuum and solution were found to differ, critically, only minor variations in the transport properties were predicted by the simulations even if trapped solvent was present.

Published under an exclusive license by AIP Publishing. <https://doi.org/10.1063/5.0091142>

## I. INTRODUCTION

Organic light-emitting diodes (OLEDs) are a key component of modern displays and have been successfully commercialized in a number of formats.<sup>1–4</sup> They are typically manufactured either through vapor deposition under vacuum or via solution processing techniques such as spin-coating, blade-coating, or ink-jet printing. Solution processed OLEDs have a number of potential advantages over their vacuum-deposited counterparts, including low embedded energy manufacturing, ease of scalability, and being less wasteful of materials during fabrication.<sup>5–10</sup> However, small molecule OLEDs fabricated using solution processing techniques are often less stable than the equivalent vacuum-deposited films.<sup>4,11–14</sup> The performance of OLEDs also varies between different solution deposition processes; for example, blade-coating has been shown to yield higher-performing films than spin-coating.<sup>14</sup> These differences in operational stability, both between different solution processing

techniques and between solution- and vacuum-deposited devices, have been attributed to differences in film morphology.<sup>4,11–14</sup> Differences in charge transport have also been observed between vacuum-deposited and solution processed small molecule OLED films, which, again, were attributed to differences in molecular packing within the film.<sup>12,15</sup> This study aims to elucidate details of these morphology differences and reveal their effects on charge transport and exciton dynamics.

The morphology at the molecular level of vacuum- and solution-deposited blend films is difficult to examine experimentally. It can, however, be analyzed computationally using molecular dynamics (MD) techniques. In particular, recent work by Lee *et al.* demonstrated that it was possible to simulate the process of solvent evaporation from the surface of a film in atomic detail.<sup>16</sup> This computational technique has allowed the generation of realistic morphologies of solution processed thin films by directly mimicking the process by which these films are formed experimentally. The

work also underlined the role of the resulting concentration gradient in determining both the mechanism of film growth and the final morphology.<sup>16</sup>

In earlier, less realistic simulation studies of solvent evaporation for film formation, systems were simulated as a uniform bulk solution containing the solute with solvent molecules being removed at random. This method resulted in a process akin to spinoidal decomposition (spontaneous uniform phase separation).<sup>17,18</sup> While spinoidal decomposition is believed to occur in some organic semiconductors, Lee *et al.* showed that for a solution containing *bis*(2-phenylpyridine)(acetylacetonate)iridium(III) [Ir(ppy)<sub>2</sub>(acac)] and 4,4'-bis(*N*-carbazolyl)biphenyl (CBP) in chloroform deposited onto a graphene surface, the film nucleated at, and grew from, the vacuum–solution interface. In addition, they showed that solvent could remain trapped in the film.<sup>16</sup> This raises questions regarding whether charge and exciton dynamics in such films differ from those in vacuum-deposited light-emitting layer blends due to the trapped solvent, and whether this might go some way toward explaining the differences in device performance and the rate of degradation observed in solution-processed films. For example, it has been suggested that degradation of small molecule phosphorescent OLEDs is due to molecular aggregation in the host material induced by exciton–polaron interactions<sup>19,20</sup> and that this process may be a root cause behind the lower electroluminescence stability of solution-processed films.<sup>11</sup> However, exactly why this degradation process would be less prevalent in vacuum-deposited films is unclear. It is possible that different transport characteristics arising from differences in film composition or morphology (e.g., less guest aggregation) could make these exciton–polaron interactions less likely in evaporated thin films. Alternatively, the presence of trapped solvent may increase the physical freedom of molecules in the film, allowing the host to aggregate more easily under operational conditions.

In this study, atomistic molecular dynamics simulations are used to obtain structures of solution- and vacuum-deposited thin films of an archetypal emissive layer blend comprised of 5 wt. % Ir(ppy)<sub>2</sub>(acac) in a CBP host. This blend was chosen as it has been well characterized computationally and is closely related to blends studied experimentally formed by both deposition techniques.<sup>11,13,14</sup> In particular, a method is introduced to enable simulated solution-processed films of greater thickness to be formed. Charge transport and exciton dynamics are then simulated under typical operating conditions using kinetic Monte Carlo (KMC) techniques. Details regarding simulation techniques and the specific systems modeled are provided in Sec. II, an analysis of results is presented in Sec. III, and concluding remarks in Sec. IV.

## II. METHODOLOGY

Both the vacuum-deposited and solution-processed films were grown on a periodic graphene substrate with lateral (*x* and *y*) dimensions of 17.04 and 16.73 nm, respectively. The MD simulations were performed at 310 K in line with previously reported protocols.<sup>16</sup> The KMC simulations were performed at 300 K, and for this reason, the morphologies were equilibrated at 300 K for at least 5 ns before the KMC simulations were initiated. The interaction parameters for CBP and the graphene substrate were identical to those used in

previous work,<sup>21</sup> and the interaction parameters for Ir(ppy)<sub>2</sub>(acac) were taken from the work of Lee *et al.*<sup>16</sup>

### A. Solution deposition

The protocol used to mimic solution deposition was based on that developed by Lee *et al.*<sup>16</sup> This involves allowing solvent molecules to evaporate spontaneously from the solution–vacuum interface. Molecules that escape from the surface of the film are removed from the system at fixed time intervals. Simulating solution deposition to provide thick films in this manner is computationally expensive due to the large number of atoms required. In order to generate a film of sufficient thickness and to accelerate drying, two modifications to the scheme of Lee *et al.*<sup>16</sup> were developed.

To increase the thickness of the final layer while maintaining a manageable number of atoms during the initial stages of the simulation, a method was developed to insert solution containing Ir(ppy)<sub>2</sub>(acac) and CBP into the system below the growing film as the solvent is lost from the surface. This process, illustrated in Fig. 1, takes advantage of observations by Lee *et al.* that the Ir(ppy)<sub>2</sub>(acac):CBP film grows from the solution–vacuum interface and that while the solute density gradient is very steep just below the growing film, its density in the lower section of the system remains almost identical to the initial solution.<sup>16</sup> In addition, the molecules in this lower section diffuse freely and show short spatial correlation times. This means that it is possible to progressively insert additional layers of solution into this region of the system, allowing thicker films to be formed at a lower computational cost without influencing the morphology of the growing film.

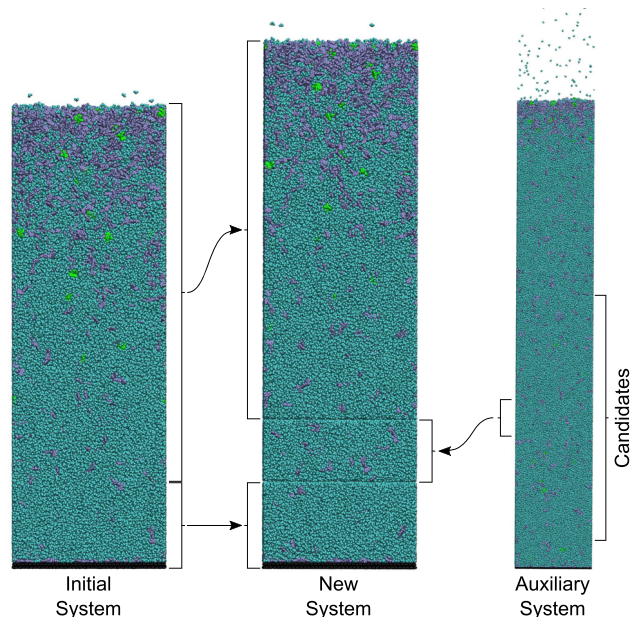


**FIG. 1.** Illustration of the layer insertion process. Black, cyan, green, and purple represent the atoms of the substrate, solvent, Ir(ppy)<sub>2</sub>(acac), and CBP, respectively, using a space filling model in the Visual Molecular Dynamics (VMD) visualization software.<sup>22</sup>

To implement this scheme, the solute density gradient was monitored during the simulation. An insertion event was performed when the bottom of the density gradient crossed below a threshold of 30 nm above the substrate (identified based on four consecutive 2.5 Å thick layers with a number density of solute atoms above  $0.01 \text{ \AA}^{-3}$ ). Note that atomic density was preferred over mass density as it can be faster to calculate after each 40 ps simulation period. Before performing the insertion, slices through the system between 5 and 15 nm above the graphene substrate were analyzed to determine where best to introduce the new section of solution. The best position was determined to be where the number of solute molecules ( $\text{Ir}(\text{ppy})_2(\text{acac})$  and CBP) in a given plane was minimal. In this study, the potential slice points ( $x$ - $y$  planes) were identified as those where the fraction of atoms from solute molecules within a 2.5 Å thick layer above the plane was below 15%. If multiple possible slice planes were identified, one was chosen at random. All molecules with at least one atom above the chosen plane were shifted in the  $z$  direction to make space for a new layer of solution to be inserted. The new section of solution was extracted from an auxiliary system as shown in Fig. 1. A layer  $6.0 \pm 1.2$  nm thick was identified using the same criteria as for identifying slicing planes described above. To avoid overlap between molecules in the two systems, any molecules from the main system that crossed the plane along which that system was sliced were removed, as were any molecules in the new solution section that had atoms crossing the upper or lower boundaries. A gap was included on either side of the new layer of solution such that the minimum distance between any inserted atom and the main system was 1.7 Å. This meant that the simulations could be restarted without the need to minimize the merged system.

The gaps introduced were sufficiently small that the new layer merged with the original system rapidly upon resuming the simulation of the drying process. This is evident in Fig. 2, which shows the density of the solvent and solute before and after an insertion event.

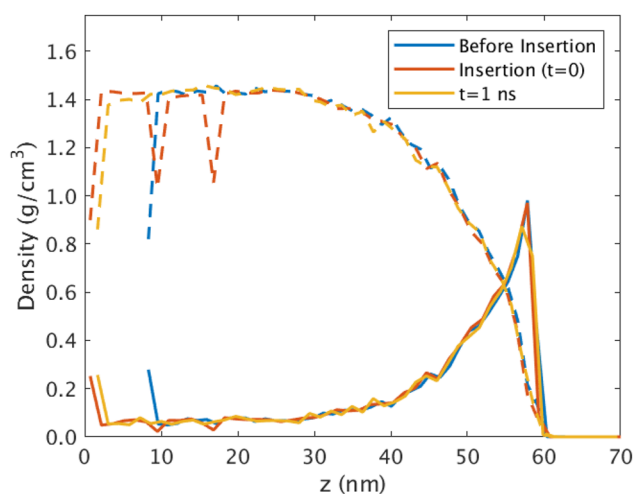


**FIG. 2.** Density of solute (solid lines) and solvent (dashed lines) 40 ps before insertion, immediately after insertion, and 1 ns after insertion. Note that the density data before insertion and 1 ns after insertion were shifted on the  $z$  axis so that the tops of the layers were aligned.

As can be seen, the density profiles in the region of the insertion ( $z = 10$ – $17$  nm) are indistinguishable from the surrounding system within 1 ns. This protocol enabled a dry film with a total height of  $\sim 13$  nm to be achieved within the computing time available. A total of 12 insertions were performed, resulting in  $\sim 30\%$  more solute atoms in the final layer than previously reported. A film of this thickness and solute content without the insertion scheme would require an initial system with  $>2.3 \times 10^6$  atoms, compared to the  $\sim 1.8 \times 10^6$  initial atoms used here. Smaller initial configurations could, in principle, also be used, noting that the simulations here were continued from the “ $t = 0.4 \mu\text{s}$ ” system of Lee *et al.*<sup>16</sup> Between insertion steps, the system typically contained between 750 000 and 800 000 atoms.

The second challenge when simulating solution deposition is obtaining an appropriate proportion of the solvent in the final layer. While it is often assumed that the amount of solvent in practical solution-deposited layers is negligible, results obtained by Lee *et al.* suggested that even on experimental time scales, as much as 5 wt. % solvent could remain trapped in the system.<sup>16</sup> This is because the rate at which the solvent can diffuse through and escape from the surface of the film decreases dramatically once the  $\text{Ir}(\text{ppy})_2(\text{acac})$  and CBP form a solid matrix. To facilitate the removal of the solvent from the system once a solid film had formed, a small quantity of the solvent was randomly deleted at regular time intervals. Up to 15 molecules could be deleted every 40 ps without affecting the shape of the solute density gradient. It should be noted that the solvent molecules removed from the film in this manner were in addition to any solvent molecules that evaporated spontaneously from the surface. The randomly selected deleted solvent molecules were at least 5 nm apart.

Initially, the only solvent molecules considered for deletion were those within a 12.5 nm section below the point at which the atomic density of the solute first exceeded  $0.04 \text{ \AA}^{-3}$ , corresponding roughly to the lower portion of the region with a large solute density gradient. This biased the selection toward solvent molecules that were already likely to reach the surface and escape, thereby accelerating the loss of the solvent without changing the structure of the film. Removal of the solvent close to the film–vacuum interface was avoided in case this caused solvent percolation pathways through the top of the film to collapse.

Once the bottom of the solute concentration gradient (defined as before by the point above which the atomic density of the solute exceeded  $0.01 \text{ \AA}^{-3}$ ) approached the substrate (within 2 nm), the number of solvent molecules deleted per 40 ps was reduced to 10, and the solute density beyond which solvent molecules were not removed (upper cut-off) was increased to  $0.08 \text{ \AA}^{-3}$ . From this point, to avoid causing the system to unphysically separate, the number of solvent molecules deleted per 40 ps was adjusted such that the probability of a given solvent molecule being deleted remained approximately constant. However, as the molar ratio of the solvent to solute approached 2:1, the motions of the solvent became heavily restricted. As the solvent was no longer able to diffuse through the layer on the time scale of the simulation, the remaining solvent molecules were removed by selecting up to 10 molecules ( $>5$  nm apart) every 40 ps from throughout the system until all the solvent was removed.

In total, around 431 000 solvent molecules were removed to form the dry film, of which  $\sim 120$  000 were inserted into the lower

section as the film dried. The first 201 000 solvent molecules evaporated spontaneously from the surface over  $0.4 \mu\text{s}$ , and it was during this time that the surface layer formed.<sup>16</sup> Beyond this point, the evaporation rate slowed dramatically. Therefore, the second removal process was turned on, whereby solvent molecules below the surface were also randomly deleted as described. Comparing the relative contribution of each removal method, we find over the entire simulation that 58% of solvent molecules were removed by evaporation, and the remaining 42% were removed by random deletion. The key points to note are that the overall rate of solvent removal slowed as the layer dried and that deletion was parameterized such that the formation and growth of the surface layer were not affected, with the solvent concentration gradient below the surface layer closely matching that obtained in runs where only surface evaporation occurred.

In addition to the fully dried film, two partially solvated films were saved for analysis to observe the effect of solvent remaining in the films. The first partially solvated film had a solvent:solute molar ratio of 1:4, which is equivalent to  $\sim 5 \text{ wt. } \%$  solvent, while the other had a ratio of 1:1 ( $\sim 17 \text{ wt. } \%$  solvent). The latter solvent content is higher than would be expected on experimental time scales, but serves to disambiguate trends related to the trapped solvent from noise in the KMC data.

## B. Vacuum deposition

The scheme used to generate the vacuum-deposited layers was identical to that described previously.<sup>21,23–25</sup> A total of eight molecules were deposited every 14 ps until the total number of molecules matched that of the systems generated by the solution deposition MD simulations. Each molecule was selected at random to be either  $\text{Ir}(\text{ppy})_2(\text{acac})$  or CBP in accordance with the target molar ratio (2:43, i.e., a guest concentration of 5 wt. %). Two separate realizations were generated, and the results from the subsequent analysis were averaged over these two realizations.

## C. Addition of transport layers

To perform the KMC simulations, transport layers were added to the solution- and vacuum-deposited light-emitting layers. These were used to isolate the emissive layer from the electrodes and allow a planar interface with the electrode. This reduces the potential for peaks on the surface of the light-emitting layer to become injection “hot spots,” and avoids the complexities of calculating electrostatic interactions involving non-planar electrodes. The transport layers were assumed to be “ideal,” meaning that (a) the injection of an electron or hole into the emissive layer was energetically favorable (yielding the maximum possible Miller–Abrahams rate), (b) the mobility of electrons and holes in the transport layer was high relative to the emissive layer, and (c) the transport layers were blocking with respect to the opposite charge and exciton diffusion.

The transport layers were simply a cubic lattice of sites between which electrons (or holes) could hop. The lattice spacing,  $a$ , was  $\sim 0.89 \text{ nm}$ . Note that to satisfy the periodic boundaries, the lattice spacing in the  $x$  and  $y$  directions differed slightly. The charge hopping prefactor,  $v_0$ , was set to  $1 \times 10^{13} \text{ s}^{-1}$  for both transport

layers [see Eq. (1) for how this affects the hopping rate calculation]. This resulted in the charge and exciton densities in the emissive layer being within a realistic range of a working OLED under typically applied fields. Hopping site energies in the transport layers were assigned randomly from a Gaussian distribution of width 50 meV.

The alignment of the electron (upper) transport layer was adjusted such that the mean distance between the centers of mass of molecules in the emissive layer and the sites in the transport layer were close to the lattice spacing at the interface. Any sites in the transport layer that were closer than this distance were removed. Full details of the scheme used to fit the upper transport layer to the emissive layer are provided in the [supplementary material](#). The hole (lower) transport layer was positioned such that the upper hopping sites were in-plane with the (deleted) graphene substrate. An example of the final morphology with upper and lower transport layers is shown in Fig. 3. Note that minor variations in the manner in which the transport layers were generated did not result in significant differences in the results from the KMC simulations (see Fig. S1 in the [supplementary material](#)).

## D. Kinetic Monte Carlo

The basic details of the KMC scheme have been described previously.<sup>21,26,27</sup> To reduce finite size effects, the films generated by MD were replicated 3 times in the  $x$  and  $y$  directions resulting in a total system area of  $\sim 2600 \text{ nm}^2$  (periodic edge length  $\sim 51 \text{ nm}$ ). Hopping sites were taken to be the center of mass (CoM) of each molecule. These sites were then assigned energy values sampled from a Gaussian distribution. For each solution-deposited morphology, three energetic disorder realizations were used. Two energetic disorder realizations were used for each of the two vacuum-deposited films. Four repeat simulations were performed for each energetic disorder realization, giving a total of

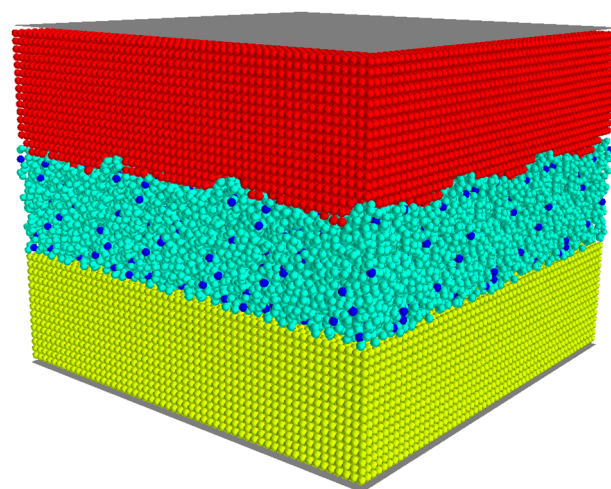


**FIG. 3.** Example morphology showing a cubic lattice transport layer fitted to the rough top surface of the light-emitting layer. Red, lime, cyan, and dark blue spheres represent the hopping sites of the electron transport layer, hole transport layer, host, and guest, respectively, and the gray planes represent the electrodes.

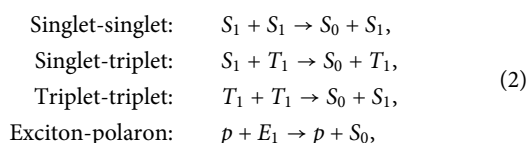
12 simulations to average over per data point for the solution-deposited systems, and 16 for the vacuum-deposited system. The error quoted is the standard deviation of the mean; however, it should be noted that as only one molecular configuration was available for each solution-deposited system, the values being averaged are to some degree correlated, and as a consequence, the uncertainty is likely to be underestimated.

Charge injection and transport were modeled using Miller–Abrahams rates<sup>39,40</sup> with a neighbor cut-off of 3 nm, as given by

$$v_{ij} = v_0 \exp(-2\gamma r_{ij}) \begin{cases} \exp\left(\frac{-\Delta E_{ij}}{k_B T}\right), & \Delta E_{ij} > 0, \\ 1, & \Delta E_{ij} \leq 0, \end{cases} \quad (1)$$

where  $v_{ij}$  is the hopping rate,  $v_0$  is the attempt to hop frequency,  $\gamma$  is the inverse localization radius,  $r_{ij}$  is the CoM to CoM distance,  $\Delta E_{ij}$  is the difference in energy between the source site,  $i$ , and the destination site,  $j$ , and  $T$  is the temperature. Coulomb interactions were handled as described by Wolf *et al.*,<sup>41</sup> with a decay parameter for the complementary error function of  $\alpha = 0.03 \text{ nm}^{-1}$ . The unit cell was reflected around the  $z = 0$  plane to ensure net charge neutrality. Site exclusion was enforced for charge hopping. That is, each polaron was prohibited from hopping to any site already occupied by another polaron of the same type. Conversely, however, any candidate hops of one polaron to a site occupied by the oppositely charged species were assumed to be energetically favorable (yielding the maximum Miller–Abrahams rate) and to result in the formation of an exciton. The formed excitons were assigned randomly to be a singlet or triplet in a 1:3 ratio. A summary of the charge transport parameters used in the KMC simulations is provided in Table I.

Exciton diffusion and interactions were modeled as described previously.<sup>21</sup> Singlets were allowed to diffuse via host-to-host and host-to-guest Förster resonant energy transfer. Triplets were allowed to diffuse via host-to-host, guest-to-guest, host-to-guest, and guest-to-host Dexter transfer, as well as guest-to-guest Förster transfer. Both radiative and non-radiative exciton decay events were considered to occur at a fixed rate dependent on the species of the occupied molecule (see Table II). Singlet decay on guest molecules was excluded, as the intersystem crossing (ISC) rate of Ir(ppy)<sub>2</sub>(acac) is much higher than the singlet decay rate.<sup>47–49</sup> Upon transfer to an occupied molecular site, exciton–exciton and exciton–polaron interactions were handled as<sup>46,57–60</sup>



where  $S_1$  and  $T_1$  represent the singlet and triplet excited states,  $S_0$  is the ground state,  $E_1$  represents either a singlet or a triplet exciton, and  $p$  represents a polaron. For simplicity, triplet–triplet annihilation (TTA) was assumed to always result in the loss of one triplet and the conversion of the other to a singlet.<sup>21</sup> In addition to quenching caused by exciton transfer events, an exciton was also quenched if an electron or hole hopped to the site occupied by that exciton (exciton–polaron quenching).

In line with previous work on *fac*-tris(2-phenylpyridine) iridium(III) (Ir(ppy)<sub>3</sub>),<sup>21</sup> the rate of triplet quenching via

TABLE I. Summary of charge transport simulation constants.

Parameter	Symbol	Value	Reference
Temperature	$T$	300 K	
Relative permittivity	$\epsilon_r$	2	26
Inverse localization radius	$\gamma$	$2.9 \text{ nm}^{-1}$	a
LUMO	$E_{\text{LUMO}}^{(\text{guest})}$	$-3.0 \text{ eV}$	28–30
	$E_{\text{LUMO}}^{(\text{host})}$	$-2.9 \text{ eV}$	31 and 32
HOMO	$E_{\text{HOMO}}^{(\text{guest})}$	$-5.6 \text{ eV}$	28–30
	$E_{\text{HOMO}}^{(\text{host})}$	$-6.0 \text{ eV}$	31 and 32
Energetic disorder	$\sigma_{\text{polarons}}^{(\text{guest, host})}$	162 meV	b
Electron hopping prefactor	$v_{0,e}^{(\text{guest})}$	$8.5 \times 10^{12} \text{ s}^{-1}$	c
	$v_{0,e}^{(\text{host})}$	$1 \times 10^{14} \text{ s}^{-1}$	33 and d
Hole hopping prefactor	$v_{0,h}^{(\text{guest})}$	$8.5 \times 10^{12} \text{ s}^{-1}$	34 and d
	$v_{0,h}^{(\text{host})}$	$6.5 \times 10^{14} \text{ s}^{-1}$	33 and d
Transport layers	$v_0^{(\text{tx})}$	$1 \times 10^{13} \text{ s}^{-1}$	e
	$\sigma^{(\text{tx})}$	50 meV	e

<sup>a</sup>For simplicity, the inverse localization radius for triplet excitons in CBP was assumed to be equal to that of Ir(ppy)<sub>2</sub>(acac). The same simplifying assumption was also used for electrons and holes on both molecules as the value of  $2.9 \text{ nm}^{-1}$  is comparable with the value of  $3.3 \text{ nm}^{-1}$  assumed in other recent KMC studies.<sup>35,36</sup>

<sup>b</sup>Energetic disorder of polaron states was assumed to be the same as that of a 6 wt. % Ir(ppy)<sub>3</sub>:CBP blend.<sup>37</sup>

<sup>c</sup>Due to a lack of experimental data, and considering the similarity in hole mobility between Ir(ppy)<sub>2</sub>(acac) and Ir(ppy)<sub>3</sub>,<sup>25,34</sup> the electron:hole mobility ratio of Ir(ppy)<sub>2</sub>(acac) was assumed to be 1:1—approximately the same as that of Ir(ppy)<sub>3</sub>.<sup>38</sup>

<sup>d</sup>Miller–Abrahams hopping prefactors were chosen to give mobility values of  $3 \times 10^{-4} \text{ cm}^2/\text{V s}$ ,<sup>33</sup>  $2 \times 10^{-3} \text{ cm}^2/\text{V s}$ ,<sup>33</sup> and  $2.4 \times 10^{-5} \text{ cm}^2/\text{V s}$ <sup>34</sup> for  $v_{0,e}^{(\text{host})}$ ,  $v_{0,h}^{(\text{host})}$ , and  $v_{0,e,h}^{(\text{guest})}$ , respectively, under single carrier transport in a neat, 46 nm thick cubic lattice film with an applied voltage such that the average electric field was  $4.9 \times 10^5 \text{ V/cm}$ .

<sup>e</sup>Transport layer parameters were chosen such that exciton densities in the emissive layer under typical electric field strengths were within the range of experimentally observed values.

dipole–dipole interactions independent of the exciton density was assumed to depend only on  $r^{-6}$ ; the inverse sixth power of the intermolecular distance (see Refs. 61–64 for discussions characterizing this process, which we will henceforth refer to as dipole–dipole quenching). The rate was equivalent to the Förster transfer rate with an additional activation energy.<sup>21</sup> Given the similarities in molecular structure and photophysical properties (photoluminescence quantum yield and lifetime) between Ir(ppy)<sub>2</sub>(acac) and Ir(ppy)<sub>3</sub>, the activation energy in these simulations was assumed to be the same as that used previously for Ir(ppy)<sub>3</sub>. Table II provides a summary of the constants used to calculate exciton event rates.

TABLE II. Summary of exciton-related simulation constants.

Parameter	Symbol	Value	Reference
Förster radius	$R_0^{(S,host-host)}$	2.7 nm	42
	$R_0^{(S,host-guest)}$	2.8 nm	a
	$R_0^{(T,guest-guest)}$	2.1 nm	43 and 44
Dexter transfer prefactor	$v_0^{(T,host)}$	$5.5 \times 10^6 \text{ s}^{-1}$	b
	$v_0^{(T,guest)}$	$4.6 \times 10^{11} \text{ s}^{-1}$	45
Triplet decay rate	$v_{\text{radiative}}^{(T,guest)}$	$5.875 \times 10^5 \text{ s}^{-1}$	c
	$v_{\text{non-radiative}}^{(T,guest)}$	$3.75 \times 10^4 \text{ s}^{-1}$	c
	$v_{\text{non-radiative}}^{(T,host)}$	$71.43 \text{ s}^{-1}$	46
Singlet decay rate	$v_{\text{radiative}}^{(S,host)}$	$1.2 \times 10^9 \text{ s}^{-1}$	47 and 48
	$v_{\text{non-radiative}}^{(S,host)}$	$8 \times 10^8 \text{ s}^{-1}$	47 and 48
Inter-system crossing rate	$v_{\text{ISC}}^{(guest)}$	$8.3 \times 10^{11} \text{ s}^{-1}$	49 <sup>d</sup>
Triplet energy	$E_T^{(host)}$	2.6 eV	50–52
	$E_T^{(guest)}$	2.3 eV	28, 34, and 53
Singlet energy	$E_S^{(host)}$	3.1 eV	e
	$E_S^{(guest)}$	2.99 eV	53
Energetic disorder	$\sigma_{S,T}^{(guest)}$	50 meV	44 and 45 <sup>f</sup>
Dipole–dipole energy quenching activation	$E_{\text{quench}}$	170 meV	g

<sup>a</sup>The Förster radius for host to guest singlet transfer was assumed to be equal to the value measured by Ruseckas *et al.* for transfers from CBP to Ir(ppy)<sub>3</sub>-cored dendrimers.<sup>47</sup>

<sup>b</sup>Triplet Dexter transfer rates in CBP were chosen such that the average triplet diffusion length was 140 nm<sup>46</sup> in a neat, fully periodic, cubic lattice system with a lattice spacing of 0.89 nm.<sup>26</sup>

<sup>c</sup>Radiative and non-radiative triplet decay rates in Ir(ppy)<sub>2</sub>(acac) were calculated from a lifetime of 1.6  $\mu\text{s}$ <sup>54,55</sup> and a photoluminescence quantum yield of 0.94.<sup>56</sup>

<sup>d</sup>The ISC rate was taken as the mean rate of the *cis*- and *trans*-isomers as calculated by Heil *et al.*<sup>49</sup>

<sup>e</sup>The singlet energy of CBP was assumed to be equal to the HOMO–LUMO gap.

<sup>f</sup>Energetic disorder of polaron states was assumed to be the same as that of a 6 wt. % Ir(ppy)<sub>3</sub>:CBP blend.<sup>37</sup>

<sup>g</sup>Modeling of the dipole–dipole quenching process has been described in detail in previous work on Ir(ppy)<sub>3</sub>.<sup>21</sup> As there was no data for the dipole–dipole quenching rate of Ir(ppy)<sub>2</sub>(acac), the Ir(ppy)<sub>3</sub> rate and activation energy were used.

### III. RESULTS

For the sake of clarity, we will first compare the structures of the simulated films. These observations will then be drawn upon to explain trends in the KMC results.

#### A. Film structure

Figure 4 shows the distribution of the guest, host, and solvent molecules in the as-deposited films. It is immediately evident that the density profiles of the vacuum-deposited film and the fully dried solution processed film are almost indistinguishable, with the only notable difference being a slightly higher guest concentration near the surface of the solution-processed film. The partially dried films also show a higher guest concentration at the surface, but this is not unexpected considering they were taken from the same deposition trajectory. As the film grows from the solution–vacuum interface, it is possible that the observed higher guest concentration in that region is simply a chance occurrence caused by an anomalously high surface guest concentration during initial nucleation. Indeed, the initial system of Lee *et al.* (and, therefore, the initial system in this work) was one of a smaller vacuum-deposited film which was replicated in the periodic directions and expanded vertically before adding the solvent,<sup>16</sup> a process which resulted in a non-uniform initial density profile of the guest. Hence, further morphology realizations with varied initial conditions would be required to draw any conclusions about this. It is clear, however, that the residual solvent is more concentrated toward the bottom of the film, and that it tends to displace CBP rather than Ir(ppy)<sub>2</sub>(acac) molecules.

It was previously shown that the size and concentration of guest molecule clusters can affect charge transport properties.<sup>26</sup> The average guest cluster size in each film was analyzed, where a cluster of size  $n$ , defined for a maximum neighbor distance  $r$ , is a group of  $n$  molecules separated by CoM to CoM hops within  $r$  nm. Figure 5 shows the mean cluster size as a function of  $r$  and Fig. 6 illustrates the distribution of cluster sizes for a maximum neighbor distance  $r = 1.4$  nm. From these two figures, it can be seen that there is no significant difference in guest clustering between the films formed from vacuum or solution deposition and in the latter case whether the films were dry or had solvent present.

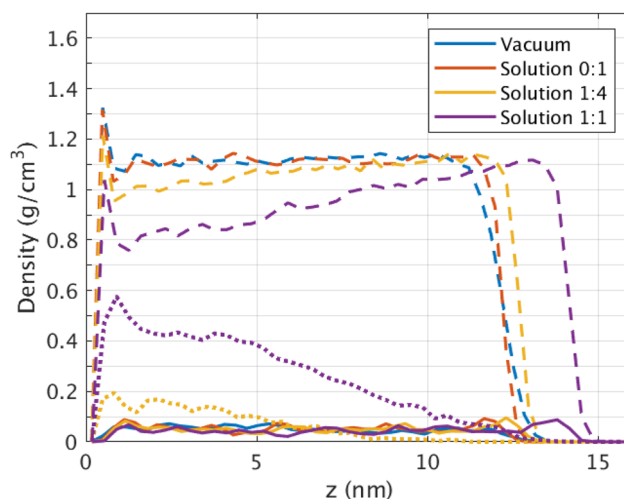
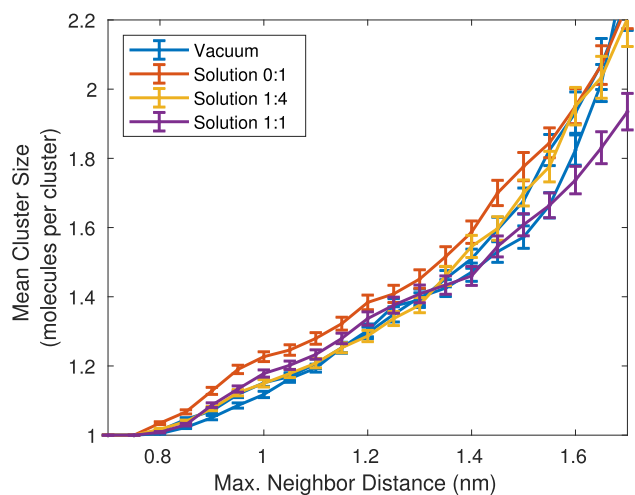
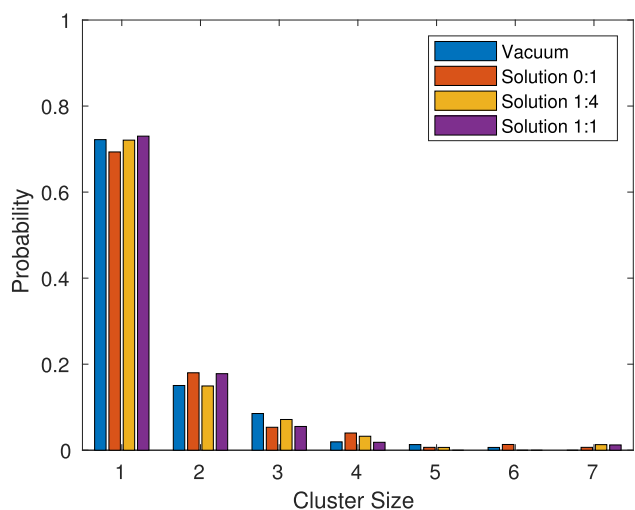


FIG. 4. Comparison of density profiles of the guest (solid lines), host (dashed lines), and solvent (dotted lines). Note that the solvent concentration is given as the solvent:solute molar ratio.



**FIG. 5.** Comparison of the average number of guest molecules in a cluster for vacuum- and solution-deposited morphologies. Data are plotted as a function of the CoM to CoM cut-off radius between neighboring molecules considered to be in the same cluster. Note that the error bars represent the standard deviation of the mean within a single morphology realization, and the two vacuum deposited morphologies are plotted separately as an indication of the expected variance between morphology realizations. Note that the solvent: solute molar ratio.

Finally, given that CBP is not spherical (has a long axis), the orientation of the host molecules with respect to the substrate was analyzed. Figure 7 shows a comparison of the orientational distribution of CBP in the bulk of the vacuum- and solution-deposited films, noting that the films were not thermally annealed. In the vacuum-deposited film, the long axis of the CBP host molecules



**FIG. 6.** Comparison of the distribution of cluster sizes for vacuum- and solution-deposited morphologies, where a cluster is a group of guest molecules connected by CoM to CoM hops between molecules of at most 1.4 nm.

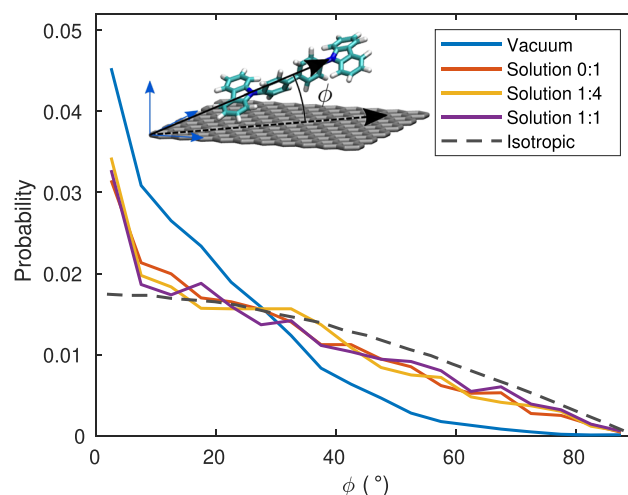


**FIG. 7.** Comparison of the probability density function of CBP orientations ( $\phi$ ) in the bulk, where  $\phi$  is the angle between the nitrogen to nitrogen vector and the substrate, as illustrated. The dashed line indicates an isotropic distribution. The bulk was defined as the section of the film between  $z = 2$  nm and  $z = 11$  nm (see Fig. S2 in the supplementary material for the distribution of angles as a function of  $z$ ). Note that these results are for films that were deposited near room temperature and had not been thermally annealed.

preferentially aligns parallel to the substrate. The molecular orientation of the solution processed film was more isotropic, although some preference for parallel alignment with the substrate was still present. Note that the distribution of CBP orientations in the solution processed film as a function of the distance from the substrate is in line with that found previously by Lee *et al.*,<sup>16</sup> suggesting that the changes in the deposition protocol introduced to enhance computational efficiency had negligible effect on the results (see Fig. S2 in the supplementary material for a plot that can be directly compared to the results of Lee *et al.*). These results are also in good agreement with the experimental work comparing vacuum-deposited and spin-coated films of tris(4-carbazoyl-9-ylphenyl)amine (TCTA).<sup>12</sup>

## B. Charge and exciton dynamics

With the addition of transport layers and electrodes as described above, KMC simulations were performed under various applied biases, which provided electric fields equivalent to working OLEDs, as summarized in Table III. Results were recorded once the system had achieved a steady state, identified by analyzing the number density profiles of charges and excitons. In the model used, the presence of excitons does not affect charge dynamics. This means that averaging of the charge transport properties could begin before the exciton concentration had reached a steady state. Simulation times were chosen such that the steady-state exciton results could be averaged over the final 50% of each simulation to achieve sufficiently converged results, and this was found to allow averaging of the steady-state charge mobility over the final 80%. Note that the length of time required to achieve a steady state depended on the field strength, and the length of time that the simulations were run varied accordingly (see Table III).

**TABLE III.** Applied electric fields and their corresponding run times.

Applied field (V/cm)	Simulation time ( $\mu$ s)
$3 \times 10^5$	40
$4 \times 10^5$	25
$5 \times 10^5$	10
$6 \times 10^5$	6

### 1. Charge transport

Mobility in the emissive layer was calculated as

$$\mu = \frac{\langle v_d \rangle}{E}, \quad (3)$$

where  $E$  is the applied electric field and  $\langle v_d \rangle$  is the average drift velocity in the direction of the field. The drift velocity was calculated using only charge hops for which both the source and destination site were in the emissive layer. Hops to or from sites in the transport layers were excluded.

The electron and hole mobilities as a function of the applied field strength are shown in Fig. 8. As can be seen, the difference in hole mobility between the vacuum-deposited film and the dry solution processed film is negligible independent of the electric field. In contrast, as the applied electric field increases there is some evidence of slower electron mobility in the solution processed films relative to that in the vacuum evaporated films. Note that trapping of electrons on the guest is relatively shallow in these systems (0.1 eV). This means that electron transport can be more host-based than hole transport, with the average electron visiting approximately twice as many host molecules as the average hole (see Fig. 9). The difference

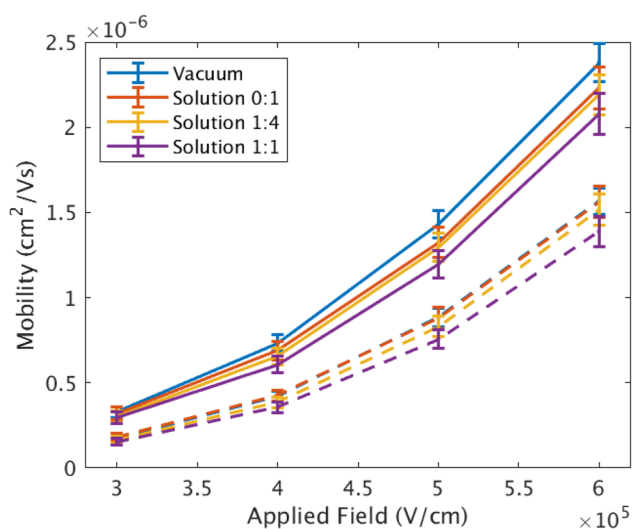


**FIG. 8.** Comparison of electron mobility (solid lines) and hole mobility (dashed lines) as a function of the applied electric field for various solvent:solute molar ratios. Note that the hole mobilities in the vacuum-deposited and 0:1 solvent:solute blends essentially overlap in the figure.

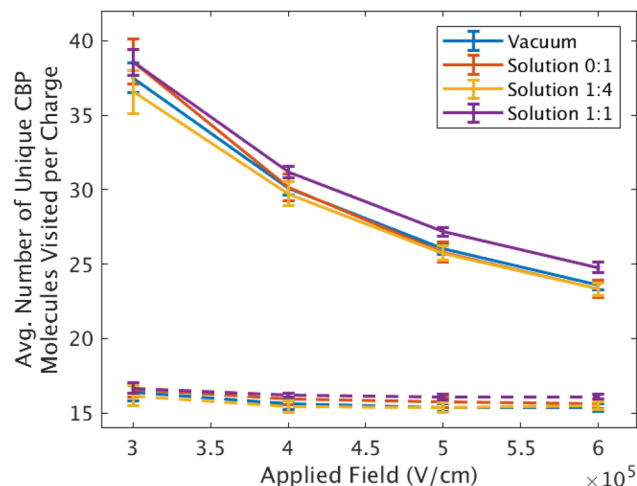


**FIG. 9.** Comparison of the average number of host molecules visited per electron (solid lines) and per hole (dashed lines).

in electron transport at high electric fields between the vacuum-deposited film and the dry solution processed film can, therefore, be explained by the difference in the degree of alignment of CBP (see Fig. 7). As charge transport was modeled as CoM to CoM hops, the higher degree of CBP alignment with the substrate observed in the vacuum-deposited film results in hops in the direction of the applied field being shorter (and hence faster) on average compared to those in the solution processed film. As electron transport has a strong host component compared to hole transport, this difference is mainly evident in the electron mobility. Note that in this work, simple distance-based criteria were used to infer the probability a hop would occur. The effects of all molecular orientations and the polarizability of the local environment were not considered. These parameters would be expected to further enhance the differences between the vacuum- and solution-deposited films.

As expected, reduced charge mobility was observed for films containing residual solvent (Fig. 8). As it was assumed that charges could not hop to or from solvent molecules in this model, trapped solvent reduces the density of available hopping sites. Indeed, Kim *et al.* have reported similar differences in current density between solution- and vacuum-deposited blends of small molecule OLED films.<sup>15</sup> They ascribed this to a lower packing density in the bulk of the solvent-derived film, despite both films having similar surface morphologies. However, the simulation studies show that the packing density of the vacuum-deposited and dry solution processed films is almost indistinguishable, as voids in the system collapse rapidly once the solvent is removed.<sup>16</sup> Thus, our results suggest that differences in electron and hole mobility observed experimentally likely, at least in part, stem from the presence of the trapped solvent decreasing the number of potential hopping sites and increasing the energetic disorder.<sup>65</sup>

It is also notable in Fig. 9 that more host molecules were visited by both electrons and holes in the film with a 1:1 solvent:solute ratio than in the other films. At first sight, this appears to contradict the lower overall charge mobilities. However, the charge mobilities are measured to be normal to the electrodes, and hence the greater

number of sites visited by charges can be attributed to greater lateral movement as they percolate through the film. This is consistent with Fig. 4, which shows that the residual solvent is concentrated toward the bottom of the film (near the hole transport layer). It is hence evident that relatively small mass-fractions of the residual solvent could still present a barrier to charge injection into, and transport through, the light-emitting layer.

## 2. Exciton dynamics

We first consider the fate of the singlet excitons that form on the host molecules. Figure 10 shows that the probability that a singlet exciton is either able to reach a guest molecule and cross to the triplet state, or is quenched by singlet–singlet annihilation (SSA, the only singlet loss process found to have a notable contribution) was not affected by the deposition process, even for high amounts of trapped solvent. However, singlet diffusion occurs via Förster transfer, which is sensitive to the degree of alignment between transition dipoles of the donor and acceptor molecules. Thus, it might be expected that the broader distribution of CBP orientations observed in the solution processed film (see Fig. 7) would in reality lead to lower transfer rates than in the vacuum-deposited film. Despite this, considering that singlet diffusion is fast compared to competing processes involving triplets or charges, and that singlets do not need to diffuse far to reach a guest molecule, it is expected that the singlet-to-triplet conversion efficiency observed here would not differ significantly from a more accurate transport model that takes into account the orientation of molecules. In addition, singlet–polaron quenching was found not to contribute significantly to singlet loss. This supports claims that exciton–polaron interaction-induced film degradation is predominantly caused by triplet–polaron quenching (TPQ).<sup>36</sup>

Triplet excitons, once formed either by singlet ISC on the guest or by charges meeting on the guest or host, were subject to several

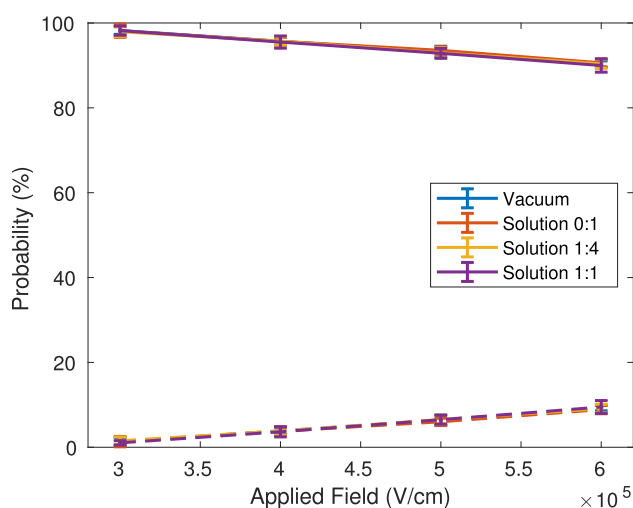


**FIG. 10.** Comparison between vacuum- and solution-deposited films on the probability that a singlet that formed on a host molecule undergoes ISC by reaching a guest molecule (solid lines) or is lost to SSA (dashed lines) as a function of the applied electric field. Note that the solvent concentration is given as the solvent:solute molar ratio.

loss processes. Significant contributions were observed from triplet–triplet annihilation, triplet–polaron quenching, and dipole–dipole quenching. Figure 11 shows a comparison of these processes between the solution- and vacuum-deposited films as a function of the applied electric field (and, therefore, the density of triplet excitons). It is notable that the difference in the probability of most processes between the solution processed and vacuum evaporated films is negligible for realistic fractions of trapped solvent (1:4 solvent:solute ratio). The main exception was dipole–dipole quenching, which was more prominent in the dry solution processed film, particularly under low electric field strength.

Given the  $r^{-6}$  distance dependence of dipole–dipole quenching, this result would be indicative of closer clustering of guest molecules in the dried solution-processed film. It is apparent from Fig. 5 that clusters of guest molecules with intercalated ligands ( $r < 1$  nm) are slightly more common in the dry solution-processed film for the particular morphology realizations obtained in this study.

Further analyzing Fig. 11, it is notable that in the case of a high solvent:solute ratio (1:1), the probability of TTA is reduced, while an increase is observed in the probability of TPQ. These differences reflect the reduced density of guest and host molecules, and are likely to be characteristic of the trend in actual devices containing trapped solvent (albeit on a smaller scale, since a 1:1 solvent:solute ratio is unrealistic). As has been observed previously in Ir(ppy)<sub>3</sub>:CBP systems,<sup>21</sup> triplet transport is almost entirely dominated by guest-to-guest Dexter transfers. Increasing the average distance between guest clusters is expected to decrease triplet diffusion, thereby reducing the likelihood of TTA. If TTA is reduced, the average lifetime of triplets would be expected to be extended (and this was, indeed, observed), leading to a higher probability

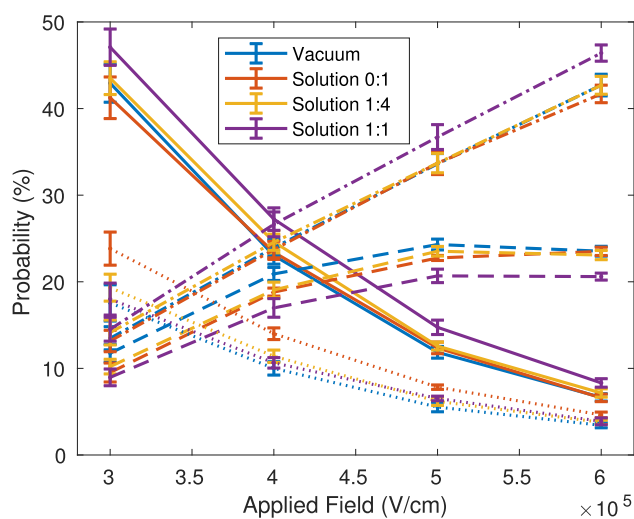


**FIG. 11.** Comparison between vacuum and solution deposited layers of the probability, as a function of the applied electric field, that a triplet decays radiatively (solid lines), is quenched via TTA (dashed lines), is quenched via TPQ (dashed-dotted lines), or is lost to dipole–dipole quenching (dotted lines). Note that for every triplet quenched via TTA, another was converted to a singlet that would quickly transition back to the triplet state via ISC. Note that the solvent concentration is given as the solvent:solute molar ratio.

of encountering a charge and being quenched via TPQ. Note that while clear differences in triplet radiative decay probability at a solvent:solute ratio of 1:1 were observed in simulations (Fig. 11), the proportion of the residual solvent in real systems is likely to be significantly lower. Overall, Fig. 11 suggests that, within the approximations of the KMC model, the relative contribution of triplet loss processes in films that have not degraded is likely to be relatively insensitive to the deposition technique. This includes the probability of TPQ, which has been suggested to contribute to film degradation.<sup>19,20</sup>

#### IV. SUMMARY

Novel molecular dynamics techniques were developed for faster simulation of film formation on a substrate by solvent evaporation. These techniques were used to simulate thicker solution processed films than have previously been achieved in atomic detail, while having negligible effect on the resultant film structure. The simulated films were a blend of 5 wt. % Ir(ppy)<sub>2</sub>(acac) in CBP, a common OLED emissive-layer blend. Using the simulated solution processed films, along with vacuum deposition simulations of the same blend, the effects on charge transport and excited state properties of the two processing techniques were compared.

It was found that for films deposited and analyzed at room temperature without thermal annealing, the CBP host molecules were preferentially aligned parallel to the substrate in the vacuum-deposited films, whereas in the solution processed films, the orientation of the CBP molecules was closer to isotropic. Despite these differences in the packing structure of the host, clustering of the guest was almost identical between the films within the margin of error.

The films were then analyzed using kinetic Monte Carlo simulations of charge transport and exciton dynamics. These simulations showed small differences in electron mobility between the vacuum- and solution-deposited films, which was associated with the differences in CBP packing. The presence of the residual solvent further reduced charge mobility normal to the electrodes by essentially diluting the available hopping sites, particularly at the bottom of the emissive layer.

It has been proposed that exciton-polaron interactions play a key role in the degradation of phosphorescent OLEDs, and that this might account for differences in the stability of the films deposited under different conditions.<sup>11,20</sup> In this study, no significant differences in exciton-polaron interactions could be detected between solution- and vacuum-deposited films with small amounts of residual solvent. Overall, the results suggest that, within the limitations of the KMC model, the deposition technique used to form the light-emitting blend films has relatively little influence on the details of charge transport and exciton dynamics. Rather, the faster degradation of solution processed films could arise from reactions of the polarons and/or excitons with the residual solvent, or from increased aggregation due to the increased physical freedom of the molecules when the residual solvent is present.

While the KMC model used in this study is a simplistic one, the agreement between our results and a range of experimentally observed phenomena<sup>12,13,15</sup> suggests that the model does

capture key elements of the processes occurring in working OLEDs.

#### SUPPLEMENTARY MATERIAL

See the [supplementary material](#) for additional supporting figures and information as indicated in the text.

#### ACKNOWLEDGMENTS

The authors wish to thank Dr. Martin Stroet and Dr. Audrey Sanzogni for their assistance in configuring the molecular dynamics simulations. The authors also wish to acknowledge the computational resources provided by the James Cook University High Performance Computing facilities and The University of Queensland's Wiener cluster. S.S. was supported by an Australian Government Research Training Program Scholarship. P.L.B. was an Australian Research Council (ARC) Laureate Fellow (Grant No. FL160100067) and is now a UQ Laureate Fellow. The work was, in part, supported by ARC (Grant Nos. DP180101421 and DP210102192).

#### AUTHOR DECLARATIONS

##### Conflict of Interest

The authors have no conflicts to disclose.

#### DATA AVAILABILITY

The data that support the findings of this study are available from the corresponding author upon reasonable request.

#### REFERENCES

- 1 Y. Im, S. Y. Byun, J. H. Kim, D. R. Lee, C. S. Oh, K. S. Yook, and J. Y. Lee, *Adv. Funct. Mater.* **27**, 1603007 (2017).
- 2 Y. Chen, J. Wang, Z. Zhong, Z. Jiang, C. Song, Z. Hu, J. Peng, J. Wang, and Y. Cao, *Org. Electron.* **37**, 458 (2016).
- 3 S.-J. Zou, Y. Shen, F.-M. Xie, J.-D. Chen, Y.-Q. Li, and J.-X. Tang, *Mater. Chem. Front.* **4**, 788 (2020).
- 4 F. Samaeifar, H. Yu, T. Davidson-Hall, M. Sadeghianlemraski, D. S. Chung, and H. Aziz, *J. Phys. Chem. C*, **125**, 20094 (2021).
- 5 K. S. Yook and J. Y. Lee, *Adv. Mater.* **26**, 4218 (2014).
- 6 M. Cai, T. Xiao, E. Hellerich, Y. Chen, R. Shinar, and J. Shinar, *Adv. Mater.* **23**, 3590 (2011).
- 7 T.-H. Han, M.-R. Choi, C.-W. Jeon, Y.-H. Kim, S.-K. Kwon, and T.-W. Lee, *Sci. Adv.* **2**, e1601428 (2016).
- 8 G. Mao, Z. Wu, Q. He, B. Jiao, G. Xu, X. Hou, Z. Chen, and Q. Gong, *Appl. Surf. Sci.* **257**, 7394 (2011).
- 9 T.-W. Lee, T. Noh, H.-W. Shin, O. Kwon, J.-J. Park, B.-K. Choi, M.-S. Kim, D. W. Shin, and Y.-R. Kim, *Adv. Funct. Mater.* **19**, 1625 (2009).
- 10 H. Ha, Y. J. Shim, D. H. Lee, E. Y. Park, I.-H. Lee, S.-K. Yoon, and M. C. Suh, *ACS Appl. Mater. Interfaces* **13**, 21954 (2021).
- 11 Y. J. Cho, S. Taylor, and H. Aziz, *ACS Appl. Mater. Interfaces* **9**, 40564 (2017).
- 12 X. Xing, L. Zhong, L. Zhang, Z. Chen, B. Qu, E. Chen, L. Xiao, and Q. Gong, *J. Phys. Chem. C* **117**, 25405 (2013).
- 13 Y. J. Cho and H. Aziz, *ACS Appl. Mater. Interfaces* **10**, 18113 (2018).

- <sup>14</sup>V. N. Hamanaka, E. Salsberg, F. J. Fonseca, and H. Aziz, *Org. Electron.* **78**, 105509 (2020).
- <sup>15</sup>H. Kim, Y. Byun, R. R. Das, B.-K. Choi, and P.-S. Ahn, *Appl. Phys. Lett.* **91**, 093512 (2007).
- <sup>16</sup>T. Lee, A. V. Sanzogni, P. L. Burn, and A. E. Mark, *ACS Appl. Mater. Interfaces* **12**, 40548 (2020).
- <sup>17</sup>C.-K. Lee and C.-W. Pao, *J. Phys. Chem. C* **118**, 11224 (2014).
- <sup>18</sup>R. Alessandri, J. J. Uusitalo, A. H. de Vries, R. W. A. Havenith, and S. J. Marrink, *J. Am. Chem. Soc.* **139**, 3697 (2017).
- <sup>19</sup>Q. Wang, B. Sun, and H. Aziz, *Adv. Funct. Mater.* **24**, 2975 (2014).
- <sup>20</sup>H. Yu, Y. Zhang, Y. J. Cho, and H. Aziz, *ACS Appl. Mater. Interfaces* **9**, 14145 (2017).
- <sup>21</sup>S. Sanderson, G. Vamvounis, A. E. Mark, P. L. Burn, R. D. White, and B. W. Philippa, *J. Chem. Phys.*, **154** 164101 (2021).
- <sup>22</sup>W. Humphrey, A. Dalke, and K. Schulten, *J. Mol. Graphics* **14**, 33 (1996); [arXiv:1503.05249v1](https://arxiv.org/abs/1503.05249v1).
- <sup>23</sup>C. Tonnelé, M. Stroet, B. Caron, A. J. Clulow, R. C. R. Nagiri, A. K. Malde, P. L. Burn, I. R. Gentle, A. E. Mark, and B. J. Powell, *Angew. Chem., Int. Ed.* **56**, 8402 (2017).
- <sup>24</sup>T. Lee, B. Caron, M. Stroet, D. M. Huang, P. L. Burn, and A. E. Mark, *Nano Lett.* **17**, 6464 (2017).
- <sup>25</sup>M. Gao, T. Lee, P. L. Burn, A. E. Mark, A. Pivrikas, and P. E. Shaw, *Adv. Funct. Mater.* **30**, 1907942 (2019).
- <sup>26</sup>S. Sanderson, B. Philippa, G. Vamvounis, P. L. Burn, and R. D. White, *J. Chem. Phys.* **150**, 094110 (2019).
- <sup>27</sup>S. Sanderson, B. Philippa, G. Vamvounis, P. L. Burn, and R. D. White, *Appl. Phys. Lett.* **115**, 263301 (2019).
- <sup>28</sup>L. Zhang, S.-C. Dong, C.-H. Gao, X.-B. Shi, Z.-K. Wang, and L.-S. Liao, *Appl. Phys. A: Mater. Sci. Process.* **118**, 381 (2014).
- <sup>29</sup>T. Xu, J.-G. Zhou, C.-C. Huang, L. Zhang, M.-K. Fung, I. Murtaza, H. Meng, and L.-S. Liao, *ACS Appl. Mater. Interfaces* **9**, 10955 (2017).
- <sup>30</sup>C. Adachi, M. A. Baldo, M. E. Thompson, and S. R. Forrest, *J. Appl. Phys.* **90**, 5048 (2001).
- <sup>31</sup>N. Matsusue, Y. Suzuki, and H. Naito, *Jpn. J. Appl. Phys., Part 1* **44**, 3691 (2005).
- <sup>32</sup>M. A. Baldo, C. Adachi, and S. R. Forrest, *Phys. Rev. B* **62**, 10967 (2000).
- <sup>33</sup>J.-W. Kang, S.-H. Lee, H.-D. Park, W.-I. Jeong, K.-M. Yoo, Y.-S. Park, and J.-J. Kim, *Appl. Phys. Lett.* **90**, 223508 (2007).
- <sup>34</sup>T. Tsuzuki and S. Tokito, *Adv. Mater.* **19**, 276 (2007).
- <sup>35</sup>H. van Eersel, P. A. Bobbert, R. A. J. Janssen, and R. Coehoorn, *Appl. Phys. Lett.* **105**, 143303 (2014).
- <sup>36</sup>R. Coehoorn, H. van Eersel, P. Bobbert, and R. Janssen, *Adv. Funct. Mater.* **25**, 2024 (2015).
- <sup>37</sup>M. A. Parshin, J. Ollevier, and M. van der Auweraer, *Organic Optoelectron. Photonics II* **6192**, 61922A (2006).
- <sup>38</sup>M. Gao, P. L. Burn, and A. Pivrikas, *ACS Photonics* **8**, 2425 (2021).
- <sup>39</sup>H. Bässler, *Phys. Status Solidi B* **175**, 15 (1993).
- <sup>40</sup>U. Wolf, V. I. Arkhipov, and H. Bässler, *Phys. Rev. B* **59**, 7507 (1999).
- <sup>41</sup>D. Wolf, P. Keblinski, S. R. Phillpot, and J. Eggebrecht, *J. Chem. Phys.* **110**, 8254 (1999).
- <sup>42</sup>R. R. Lunt, N. C. Giebink, A. A. Belak, J. B. Benziger, and S. R. Forrest, *J. Appl. Phys.* **105**, 053711 (2009).
- <sup>43</sup>E. B. Namdas, A. Ruseckas, I. D. W. Samuel, S.-C. Lo, and P. L. Burn, *Appl. Phys. Lett.* **86**, 091104 (2005).
- <sup>44</sup>L. Zhang, H. van Eersel, P. A. Bobbert, and R. Coehoorn, *Chem. Phys. Lett.* **662**, 221 (2016).
- <sup>45</sup>A. Ligthart, X. de Vries, L. Zhang, M. C. Pols, P. A. Bobbert, H. van Eersel, and R. Coehoorn, *Adv. Funct. Mater.* **28**, 1804618 (2018).
- <sup>46</sup>N. C. Giebink, Y. Sun, and S. R. Forrest, *Org. Electron.* **7**, 375 (2006).
- <sup>47</sup>A. Ruseckas, J. C. Ribierre, P. E. Shaw, S. V. Staton, P. L. Burn, and I. D. Samuel, *Appl. Phys. Lett.* **95**, 183305 (2009).
- <sup>48</sup>Y. Kawamura, H. Yamamoto, K. Goushi, H. Sasabe, C. Adachi, and H. Yoshizaki, *Appl. Phys. Lett.* **84**, 2724 (2004).
- <sup>49</sup>A. Heil, K. Gollnisch, M. Kleinschmidt, and C. M. Marian, *Mol. Phys.* **114**, 407 (2016).
- <sup>50</sup>X. Ren, J. Li, R. J. Holmes, P. I. Djurovich, S. R. Forrest, and M. E. Thompson, *Chem. Mater.* **16**, 4743 (2004).
- <sup>51</sup>A. Endo and C. Adachi, *Chem. Phys. Lett.* **483**, 224 (2009).
- <sup>52</sup>C. Adachi, R. C. Kwong, P. Djurovich, V. Adamovich, M. A. Baldo, M. E. Thompson, and S. R. Forrest, *Appl. Phys. Lett.* **79**, 2082 (2001).
- <sup>53</sup>L. Zhang, H. van Eersel, P. A. Bobbert, and R. Coehoorn, *Chem. Phys. Lett.* **652**, 142 (2016).
- <sup>54</sup>S. Lamansky, P. Djurovich, D. Murphy, F. Abdel-Razzaq, R. Kwong, I. Tsyba, M. Bortz, B. Mui, R. Bau, and M. E. Thompson, *Inorg. Chem.* **40**, 1704 (2001).
- <sup>55</sup>S. Reineke, T. C. Rosenow, B. Lüssem, and K. Leo, *Adv. Mater.* **22**, 3189 (2010).
- <sup>56</sup>M. Schmid, T. Morgenstern, and W. Brütting, *Org. Electron.* **62**, 216 (2018).
- <sup>57</sup>E. J. W. List, U. Scherf, K. Müllen, W. Graupner, C.-H. Kim, and J. Shinar, *Phys. Rev. B* **66**, 235203 (2002).
- <sup>58</sup>S. M. King, D. Dai, C. Rothe, and A. P. Monkman, *Phys. Rev. B* **76**, 085204 (2007).
- <sup>59</sup>R. Coehoorn, L. Zhang, P. A. Bobbert, and H. van Eersel, *Phys. Rev. B* **95**, 134202 (2017).
- <sup>60</sup>J.-L. Brédas, D. Beljonne, V. Coropceanu, and J. Cornil, *Chem. Rev.* **104**, 4971 (2004).
- <sup>61</sup>J. C. Ribierre, A. Ruseckas, K. Knights, S. V. Staton, N. Cumpstey, P. L. Burn, and I. D. Samuel, *Phys. Rev. Lett.* **100**, 017402 (2008).
- <sup>62</sup>T. Tsuboi and N. Aljaroudi, *Opt. Mater.* **30**, 1375 (2008).
- <sup>63</sup>Y. Kawamura, J. Brooks, J. J. Brown, H. Sasabe, and C. Adachi, *Phys. Rev. Lett.* **96**, 017404 (2006).
- <sup>64</sup>Y. Q. Zhang, G. Y. Zhong, and X. A. Cao, *J. Appl. Phys.* **108**, 083107 (2010).
- <sup>65</sup>P. Friederich, A. Fediai, J. Li, A. Mondal, N. Kotadiya, G. D'Avino, F. Symalla, G. J. Wetzelaer, D. Andrienko, D. Beljonne, P. Blom, J. L. Brédas, and W. Wenzel, [arXiv:1908.11854](https://arxiv.org/abs/1908.11854) (2019).